**ORIGINAL PAPER**

# On creep behavior of mudstone in the Tianshui area, China

Zhang Zelin[1] · Tao Wang[2]

## Abstract

The mudstone has low bearing capacity and low per Zelin meability, which experiences large deformation and long-term creep. To investigate the creep characteristics of the Tianshui Landslide, Gansu Province, China, triaxial creep tests were conducted. It is shown that the creep behavior of mudstone became more pronounced as the confining pressure, water content, and shear stress level increased. The long-term strength of the mudstone decreased as the creep time increased. A new creep model for the mudstone is proposed. The values predicted by the new model are in good agreement with the test results. The axial strain in the mudstone samples exhibited a linear relationship with time in a log–log graph under different stress states; the strain increased slowly with time and gradually stabilized. The model reflects the residual creep characteristics of the mudstone and can reflect both axial and volumetric creep. Moreover, the microscopic mechanism of clay creep was studied by analysis of scanning electron microscope images. This study considered the actual engineering situation, and the experiment was designed to study steady creep of mudstone under low confining pressure and variable water contents, with the aim of establishing a stable creep model to characterize the mudstone under low confining pressure. The stress–strain–time model of creep deformation of mudstone established herein has few parameters and a simple derivation process and provides new information for evaluating slope long-term stability. The model will be useful for the prediction of mudstone landslides in the Tianshui area.

**Keywords** Tianshui mudstone · Creep behavior · Strain–time curves · Creep model

## Introduction

Creep reduces mudstone strength and affects the long-term stability of engineered structures on or within the rock (Jiang et al. 2014; Yu et al. 2015; Wen and Jiang 2017; Li and Yang 2018; Zhang et al. 2015). As a result of creep, many landslides undergo long-term, slow deformation under the action of gravity and other internal and external geological forces (Sun et al. 2016; Wen and Jiang 2017). Many structures are built on mudstone, which has low bearing capacity, low permeability, large deformation, and strong creep characteristics, resulting in a high occurrence of landslides. Creep-induced landslides cause damage to buildings and infrastructure in the landslide area during the creep stage; moreover, a large number of creep landslides evolve into rapidly sliding landslides after long-term slow deformation, causing more serious human and economic losses (Bizjak and Zupančič 2009). Hence, systematic study of the creep characteristics of the rock and soil masses at creep landslide sites is of great importance to understand the evolution and long-term safety evaluation of such landslides (Pellet et al. 2005; Bonini et al. 2009; Rutter and Green 2011; Bozzano et al. 2012; Gasc-Barbier et al. 2004; Sun et al. 2016).

Weathered mudstone is basically similar to clay. Boom Clay also exhibits creep. Giraud and Rousset (1996) studied the time-dependent behavior of clay and found an obvious movement that increased under conditions of high water content. Yu et al. (2015) performed a series of creep tests to clarify the mechanism governing the development of creep deformation under hydro-mechanical coupling in Boom Clay. They found that the delayed creep behavior of Boom Clay became more pronounced as the deviatoric stress increased and that the creep rate depended on the deviatoric stresses. During triaxial creep tests, the creep rate of

✉ Zhang Zelin
249133236@qq.com

Tao Wang
58227005@qq.com

1  China Agricultural University, Beijing 100083, China

2  Chinese Academy of Geological Sciences Institute
of Geomechanics, Beijing 100081, China

Boom Clay reached a constant value after a certain period in most of the loading steps. Cui et al. (2009) performed high-pressure tests at controlled temperatures and found that full consolidation of Boom Clay requires a long period of time and that it is difficult to distinguish consolidation and creep from the total volume change. Coll et al. (2006) conducted a series of creep tests on Boom Clay under "open drainage" conditions with no fluid contact. However, those hydromechanical creep tests detected no significant influence of water type or stratigraphic orientation on the behavior of Boom Clay.

The creep behavior of clayey soil in the residual state and its relationship to the gravel content of the soil may be related to the strength recovery and crushing of gravel-sized particles during creep (Wen and Jiang 2017). The creep compaction behavior of crushed mudstone is highly dependent on the original grain composition and the axial stress applied to the samples. Samples containing greater numbers of large particles were more readily deformed during initial loading, because of the large voids present in the samples, and exhibited greater stability than samples with smaller particles when the axial stress was less than the bearing capacity of the ''framework structure'' of the sample (Guo et al. 2019).

Usually, clay creep exhibits three stages: (1) transient creep, in which the strain rate decreases; (2) secondary creep, in which the strain rate is constant; and (3) tertiary creep, in which the strain rate increases. Most constitutive models of rock and soil creep are empirical models or element models (Adaehi et al. 2005; Enomoto et al. 2015; Wang et al. 2019; Wang et al. 2020). The empirical models, such as the Singh–Mitchell model and Mesri model (Singh and Mitchell 1968; Mesri et al. 1981; Mesri and Choi 1984), are based on the empirical formula of stress–strain–time correlation obtained from the analysis of creep data for a rock and soil mass. Under different test conditions, different materials yield different empirical formulas. The element models, such as the Kelvin model, H–K model, Bingham model, Burgers model, and Nishihara model (Sun et al. 2016; Bozzano et al. 2012; Gao et al. 2012; Wang et al. 2016), are derived from specific theoretical formulations; however, the constitutive equations are complex, and representation of multi-parameter models is difficult.

Wang et al. (2018) performed triaxial rheological tests on mudstones from the soft interlayer in the Three Gorges Reservoir Area. They studied the mudstones under both dry and saturated conditions. A HKCV model adopts the one-dimensional and three-dimensional equations that are derived, and the HKCV model is relatively consistent with the observations of the triaxial rheological test. Wang et al. (2021) investigated the long-term stability of engineering supporting structures for landslides and the deformation control and stability prediction of rock slopes by triaxial creep tests. They discussed the creep viscosity coefficient in the accelerated creep stage and proposed a new model for creep based on the Burgers model. The proposed model fitted the test data well for all three creep stages. A creep model for unsaturated reticulate red clay under matric suction was established by Li and Yang (2018) to predict the creep strain caused by matric suction.

Up to now, a comprehensive quantitative study on the creep mechanism of mudstone in Tianshui area is still unseen, and the effect of creep behavior on the mudstone landslide evolutional process is also poorly understood. The weathered mudstone has a high viscosity and is classified as hard clay (Zhang et al. 2017a, b, c). The purpose of this study is to understand the creep behavior of clays, which may be useful to predict the landslide evolutional process. To serve this purpose, a number of creep tests were performed on weathered mudstone obtained from a typical landslide (Zhaojiazui) site in Tianshui, Gansu province of China. By considering the actual engineering situation, we designed an experiment to study the steady creep of mudstone under low confining pressure and different water contents and established a stable creep model to characterize the mudstone under low confining pressure. Finally, the mechanical properties of creep in Tianshui Tertiary mudstone to assess the long-term stability of mudstone slopes were studied. The stress–strain–time model of creep deformation of mudstone established in this paper has few parameters and a simple derivation process, represents a new means of evaluating slope long-term stability, and will be useful for landslide prediction.

## Engineering geological background

Tianshui city is located in the southwestern region of the Loess Plateau in China. The Fenghuangshan active fault runs through the study area, with a WNW–ESE strike (Fig. 1). The fault is a sinistral strike-slip fault, and has been slipping laterally at an average rate of 1.1 mm/a since 6.4 ka and vertically at an average rate of 0.37 mm/a during 16.6–6.4 ka (Zhang et al. 2017b). The landforms around Tianshui are hilly loess, and the terrain is higher in the northwest and lower in the southeast. The elevation of the Tianshui basin ranges from 750 to 2700 m, with a mean value of 1329 m; the slope gradient is 0° to 35°, with a mean value of 26.5°. The main rivers in the region are the Xihe River and its tributaries. The main rock types are loess and mudstone of Neogene age. Holocene loess is exposed mainly in low-lying areas at the feet of slopes. A Pleistocene loess layer approximately 2–6 m thick occurs in gullies; the loess has a loose structure, coarse particles, and joint fissures. The Neogene mudstone is low-permeability
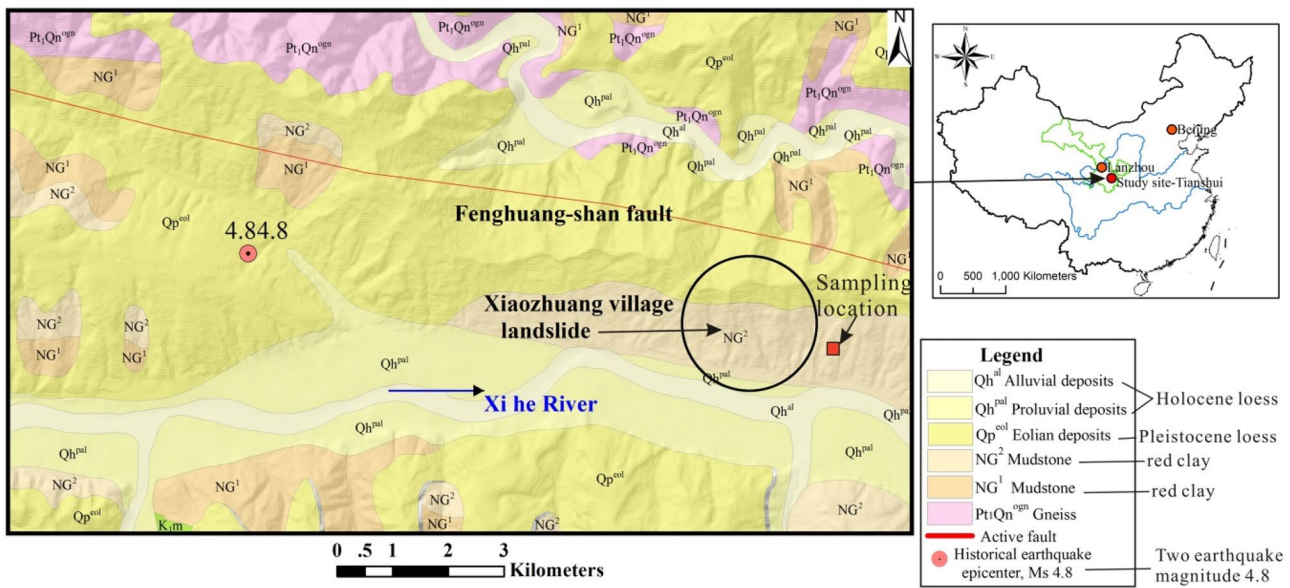
**Fig. 1** Engineering geological settings of the study area

red clay that is easily weathered and is vulnerable to creep deformation.

## Materials and testing methods

### Materials and samples

The Neogene mudstone in the Tianshui area, northwest China, contains kaolinite and smectite, with some chlorite and illite and a small amount of interlayered illite/smectite (Wen and He 2012). The mudstone is easily weathered and has low permeability. The mudstone is hard clay and forms a slippery stratum that affects the stability of the slope (Fig. 2a, b). The mudstone samples were obtained from 20-m-deep boreholes drilled into the natural slope below Tianshui city (Fig. 2c). The cores were sealed on site, transported to the laboratory, and stored under constant temperature and humidity.

The water content was measured in the field, and other parameters were measured in the laboratory. The shear modulus Gs and shear strength were measured by consolidation undrained tests. The measured Gs and shear strength are undrained parameters. The physical parameters of the mudstone are listed in Table 1, and the grain-size curves are shown in Fig. 3. The grain-size distributions of the clay were obtained by hydrometer tests. The mudstone consisted mainly of clay (ca. 80%, Fig. 3) with some silt (ca. 20%). Based on these parameters, the mudstone is classified as clay. The specimens are 200 mm high and 100 mm in diameter, with a height to diameter ratio of 2.

### Triaxial creep test program

The creep tests were performed in a YLSZ150-3 stress control triaxial creep apparatus (Fig. 4) composed of several systems: vertical loading and surrounding pressure loading; voltage stabilization; a control system; a three-axis pressure chamber; a reaction frame; a displacement and volume variable measurement system; and a load sensor and data acquisition system. To provide stable axial pressure, the instrument is equipped with a specially regulated high-pressure energy storage tank. The temperature $(20 \pm 1.5 \,^{\circ}\text{C})$ and humidity were kept constant during all the tests.

Drained creep triaxial tests were conducted at three w levels ($w = 11.0\%$, $18.0\%$, and $25.2\%$), four pressure levels ($\sigma_3 = 0.4$, $0.8$, $1.2$, and $1.6$ MPa) and four stress levels (SL = 20%, 40%, 60%, and 80% of the shear strength). The stress level (SL) is defined as the ratio of the creep stress with respect to the strength at the corresponding confining stress (Sun et al. 2016). During the test, the specimen axial pressure was held constant with a precision of $\pm 10$ kPa. The axial deformation was the measurement criterion of the test, and the interval for each deviatoric stress increment (creep stage) was 12 days (288 h). Various confining pressures and water contents were applied in the creep tests, as listed in Table 2.

### Scanning electron microscopy

Imaging by a scanning electron microscope (SEM) provides direct characterization of microstructures at the particle/aggregate scale
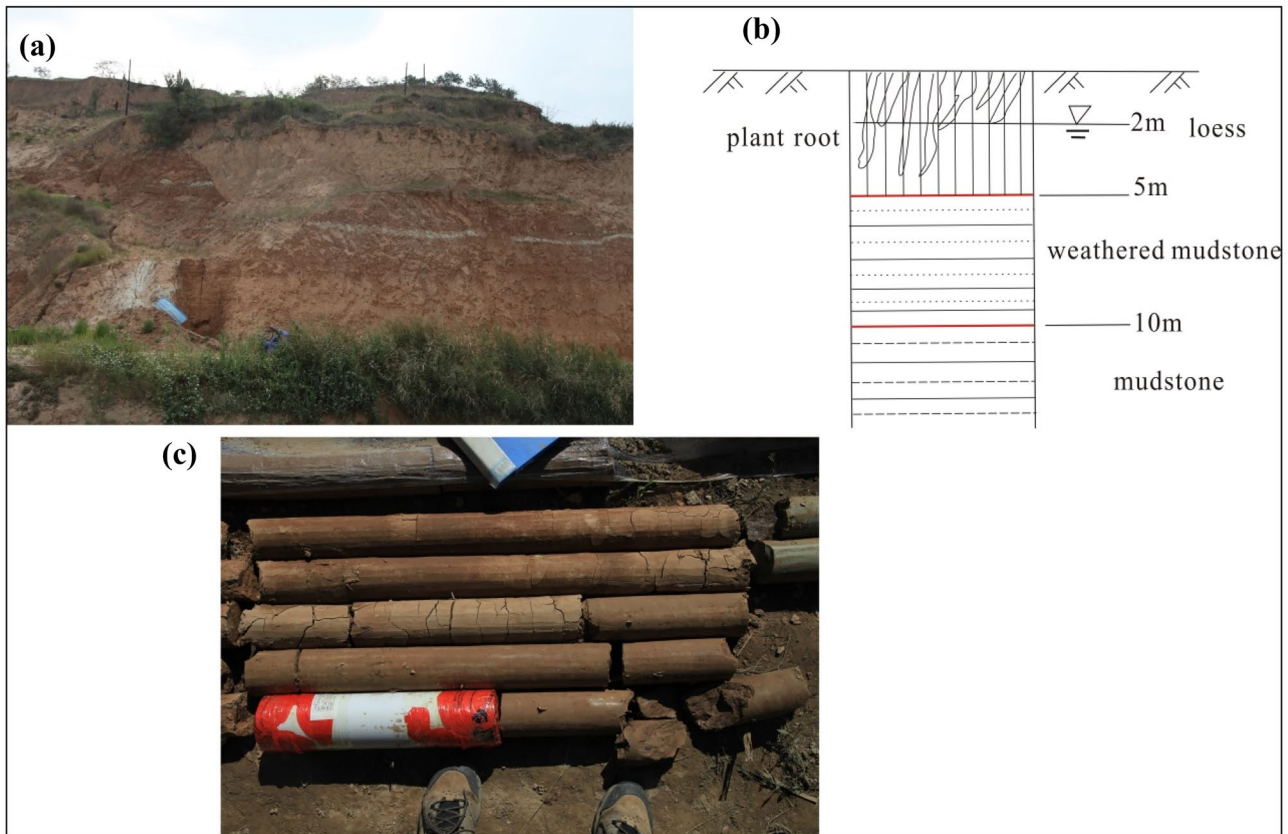
Fig. 2 The mudstone in Tianshui area, China. **a** Mudstone slope. **b** Stratigraphic section. **c** Sampling in drill cores

($< 100$ μm). In soils, these images provide useful information to examine mechanical responses at the macroscopic scale that depend on microscopic characteristics (Romero and Simms 2008; Wen and Aydin 2003). The microstructures of the undisturbed clay and sheared clay were examined here using such SEM images.

Specimens were dried before SEM examination, followed by preparation of a sample to obtain a fresh surface for imaging. A prismatic specimen ($1 \times 1 \times 0.1$ cm) was made from each compacted sample using a knife, and air-dried in a desiccator (20% relative humidity at 25 °C) for 4 weeks (Lin and Cerato 2014). Then the specimen was sputtered with gold–palladium alloy. SEM micrographs were obtained at a magnification of $2500 \times$, which allowed observation of the arrangement of the clay structure (Al-Rawas and McGown 1999). To avoid perspective distortion, specimens were placed normal to the probe (Sergeyev et al. 1980).

## Test results

### Creep tests

At each loading step, the deviatoric stress was kept constant for 288 h with the axial strain continuously recorded. The graded loading curves obtained by the creep test under different confining pressures and moisture contents are plotted in Fig. 5 and the axial strain–time curves under different water contents ($w$) and σ3 are illustrated in Figs. 6 and 7, respectively.

The triaxial creep testing was conducted under undrained conditions. The results indicate that the mudstone exhibits the typical characteristics of a stable creep material. Under each axial load, the mudstone shows three stages of deformation: instantaneous elastic–plastic deformation; attenuated deformation; and steady deformation. During instantaneous elastic–plastic deformation, as a result of the rapid increase of the axial load, the particle framework in the mudstone is subjected to load increase, resulting in elastic deformation of the particles and plastic deformation caused by positional adjustments between the particles. Macroscopically, the axial strain of the mudstone increases rapidly. During the attenuation deformation stage, the stress chain in the mudstone framework tends to be stable. The particle deformation and position adjustment decrease gradually, and the creep rate of the mudstone also decreases gradually. In the steady deformation stage, the stress chain of the mudstone skeleton is basically stable, and the macroscopic deformation of the mudstone is slow and stable.

**Table 1** Physical parameters of the weathered mudstone (mean value)

| Number | $w$ % | $Gs$ | $\rho$ g/cm³ | $\rho_d$ g/cm³ | $e$ | $LL$ | $PL$ | $PI$ | Classification | $Es_{1-2}$ MPa | $C_{cq}$ kPa | $\varphi_{cq}$ ° |
|--------|-------|------|--------------|----------------|-----|------|------|------|----------------|----------------|--------------|------------------|
| 1 | 10.2 | 2.7 | 2.02 | 1.83 | 0.47 | 38.9 | 18.8 | 20.1 | Clay | 38.3 | 120.7 | 28.5 |
| 2 | 11.3 | 2.7 | 2.15 | 1.93 | 0.39 | 40.0 | 16.5 | 23.5 | Clay | 40.5 | 125.2 | 29.1 |
| 3 | 11.5 | 2.71 | 2.13 | 1.91 | 0.42 | 42 | 17.6 | 24.4 | Clay | 41.1 | 126.4 | 29.7 |

The absolute creep variable of the mudstone, i.e., the difference between the deformation at the end of the test and the instantaneous elastic–plastic deformation, is positively correlated with the axial stress (Figs. 6 and 7). For example, at $w = 10.2\%$ and $\sigma_3 = 0.8$ MPa, the corresponding absolute creep variables at SL = 0.2, 0.4, 0.6 and 0.8 were 0.57%, 1.03%, 1.36% and 1.95%, respectively (Fig. 6a). At SL = 0.8 and σ3 = 0.4, 0.8, 1.2 and 1.6 MPa, the corresponding absolute creep variables were 1.63%, 1.97%, 2.31% and 2.72%, respectively (Fig. 7). Moreover, at $\sigma_3 = 0.8$ MPa, the corresponding absolute creep variables at $w = 11.0\%$, 18.0% and 25.2% were 1.95%, 2.74% and 3.88%, respectively (Fig. 6). These data show that the absolute creep of mudstone is affected by $\sigma_3$, $w$, and SL, that is, absolute creep is positively correlated with the axial stress value, $\sigma_3$, and $w$.

We also obtained the curves of creep strain rate vs. stress level for the mudstone samples with different values of $\sigma_3$, $w$, and SL (Fig. 8). The results demonstrate that the stable creep rate of the mudstone is also related to σ3, w, and SL, that is, the stable creep rate increases linearly with increasing axial stress. From this finding, it can be inferred that the creep strain rate depends on the deviatoric stresses. Similar observations were reported in earlier studies: the higher the load, the higher the creep strain rate (Gasc-Barbier et al. 2004; Naumann et al. 2007; Yu et al. 2015).

The isochronous stress level–strain curves are shown in Figs. 9 and 10. The isochronal curve method was used to determine the long-term strength of the mudstone. The isochronous curve shows the stress levels and strain relations at a certain time under a certain confining pressure (Yan et al. 2008; Sun et al. 2016). Under a given confining pressure, a series of measurements at various times t (such as 2, 8, 20 h) is selected from the creep curves at different stress levels to form the vertical line of the time axis. A series of stress and strain values can be obtained from the intersection point of the vertical and creep curves. As the stress level increases, the soil strain–stress curves evolve into a hyperbola. All the curves have double inflection points. The long-term strength of the mudstone, defined as the inflection point in the isochronous stress level–strain curve (Yan et al. 2008), can be estimated as 0.60–0.75 of the instant strength. Thus, we conclude that the long-term strength decreased as the creep time increased up to 196 h (Figs. 9 and 10).

## Microscopic characteristics of creep

Scanning electron microscope images were used to examine the microstructure of the undisturbed red clay and features of the shearing surface after the creep tests. Images of the undisturbed clay (Fig. 11a, b) and clay after creep testing (Fig. 11c, d) at magnifications of 500 × and 2000 × are provided. The undisturbed clay consists mainly of small aggregates with dispersed inter-aggregate pores.

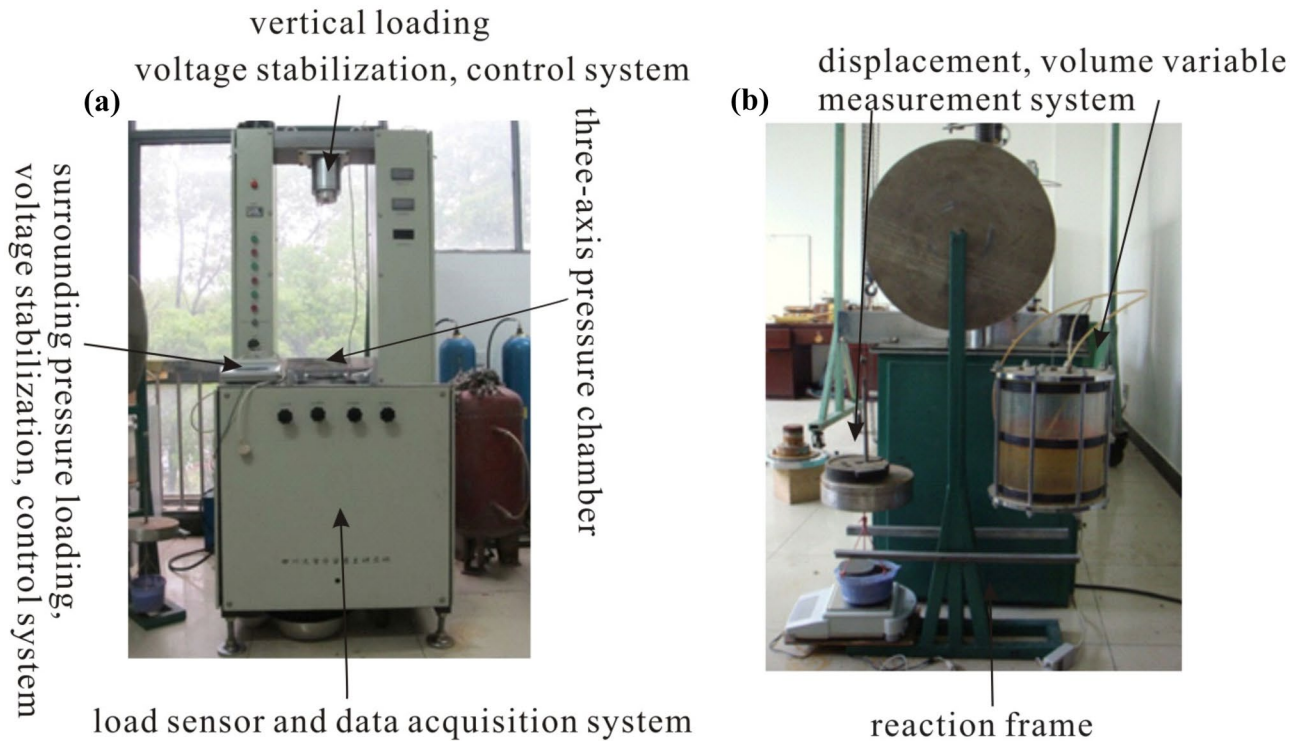**Fig. 3** Grain distribution of the mudstone
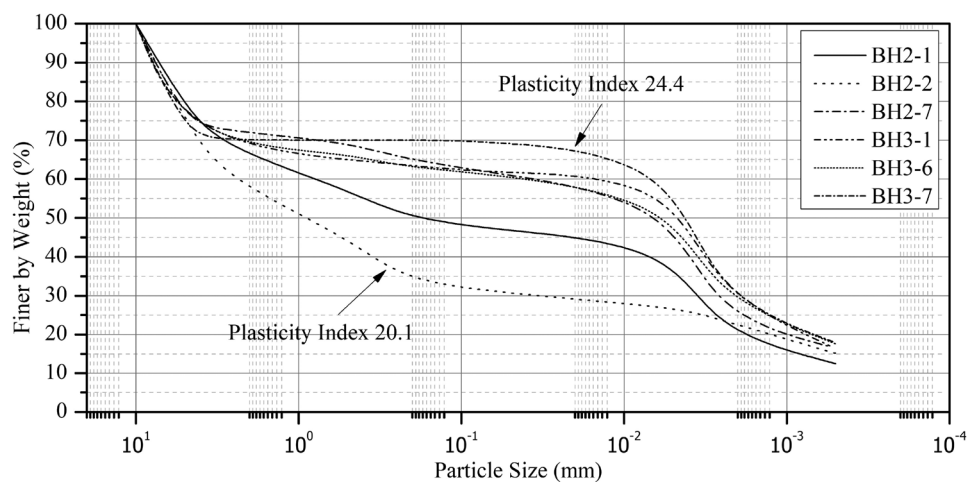
**Fig. 4** Triaxial creep apparatus. **a** YLSZ150-3 stress-controlled machine. **b** External variable measuring device

Higher porosity can be observed in the undisturbed clay, along with evidence of the aggregates being in contact with neighboring particles by cementing bonds. The microscopic features show the development of Carnisaw soil structures, with a flocculated structure dominated by edge-to-face particle associations. Moreover, there is no distinct structural anisotropy with preferential particle orientation in the undisturbed clay.

After the creep shear test, differences in the fabric between the samples are evident (Fig. 11c and d). After the first monotonic shear test, the clay fabric exhibits a relatively uniform pore distribution, whereas particles in the undisturbed sample are grouped in connected assemblages. The clay after testing has a more homogeneous structure

than the undisturbed clay. Linear striations are well developed on the shear surface, and the clay pores present a more uniform distribution than in the undisturbed clay. The loading effect dissolves the clay aggregates, leading to particle size reduction. Thus, the clay microstructure aggregate becomes dense, indicating a shearing–grinding mode of deformation.

From the SEM results, the creep behavior can be explained as follows: under long-term loading, the soil mineral particles or mineral clusters continuously slide and rotate with time, and their spatial positions are constantly adjusted. Thus, the creep mechanism in the mudstone samples is mainly related to the relative movement and rotation of the microscopic particles. As uneven stress

**Table 2** Triaxial creep test conditions

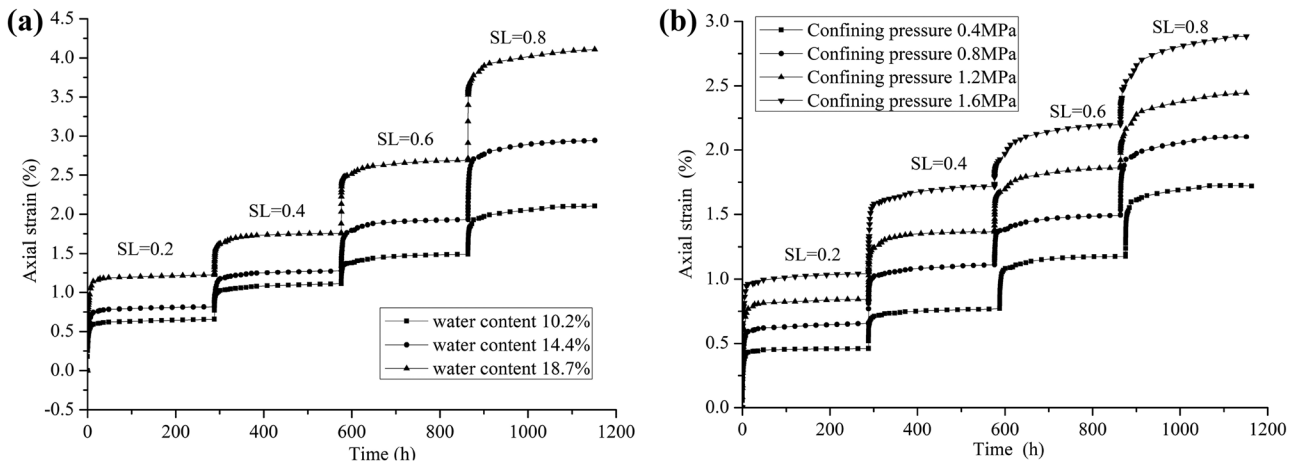| Test condition | Dry density (g/cm$^3$) | Confining pressure (MPa) | Stress level | Stable time (hour) | Sample number |
|---|---|---|---|---|---|
| Natural water content (water content 11.0%) | 1.80 | 0.4 | 0.2/0.4/0.6/0.8 | 72/72/72/72 | N1 |
| | | 0.8 | | 72/72/72/72 | N2 |
| | | 1.2 | | 72/72/72/72 | N3 |
| | | 1.6 | | 72/72/72/72 | N4 |
| Saturation condition (water content 25.2%) | 1.79 | 0.8 | | 72/72/72/72 | N5 |
| Intermediate water content (18.0%) | 1.79 | 0.8 | | 72/72/72/72 | N6 |

**Fig. 5** Relation between axial strain and time. **a** For different water contents, confining pressure 0.8 MPa; and **b** different confining pressure, natural water content

fills the soil pores, the porosity of the soil continues to decrease, and at the macroscopic level, the creep rate increases.

Based on the microscale analyses, this section discusses the shapes of internal microdefects after creep failure. The samples were selected along the surface of the shear zone
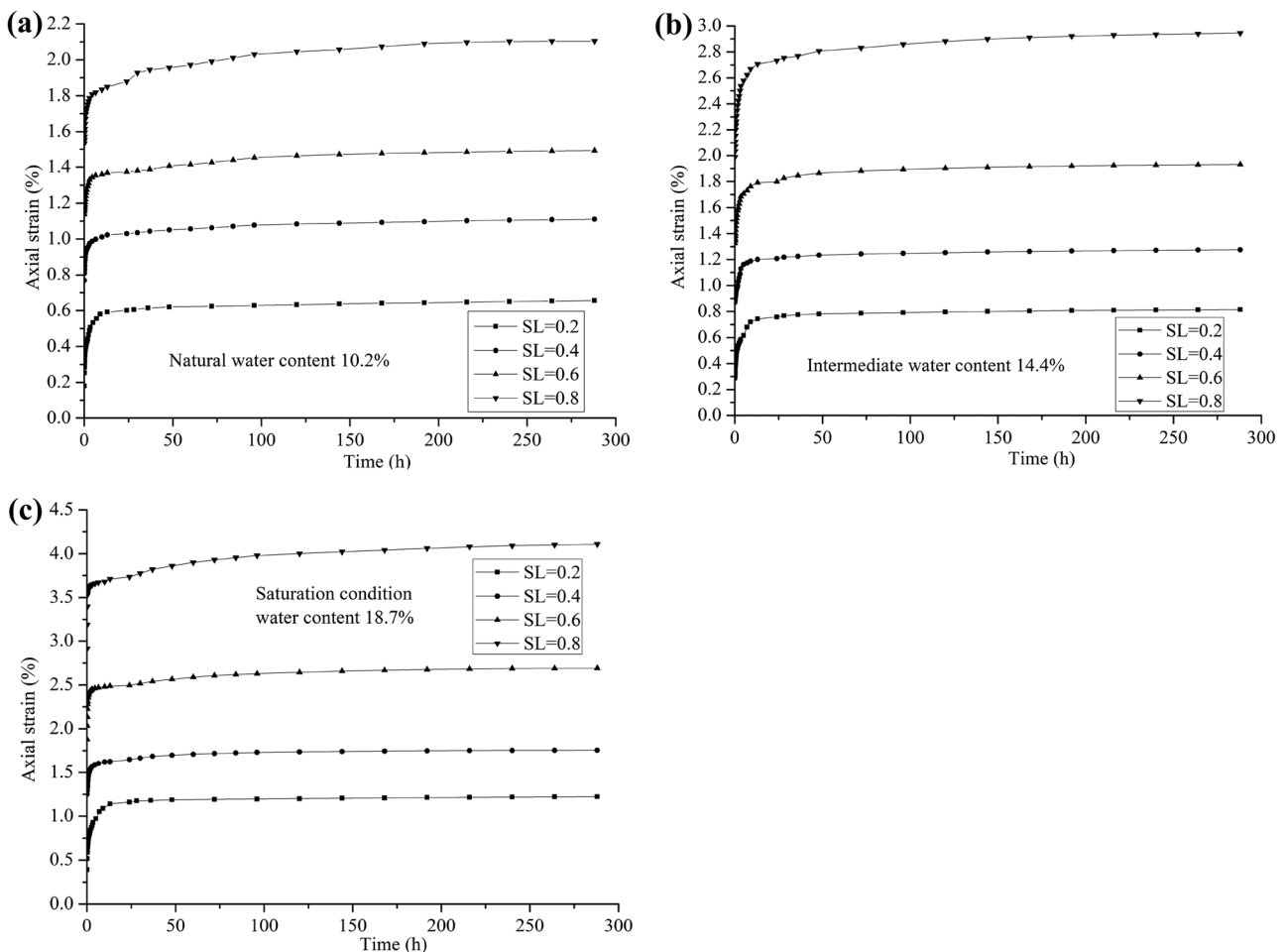


**Fig. 6** Strain–time relationship curves of triaxial creep tests (confining pressure 0.8 MPa). **a** Water content 11.0%, sample N2; **b** water content 18.0%, sample N5; and **c** water content 25.2%, sample N16
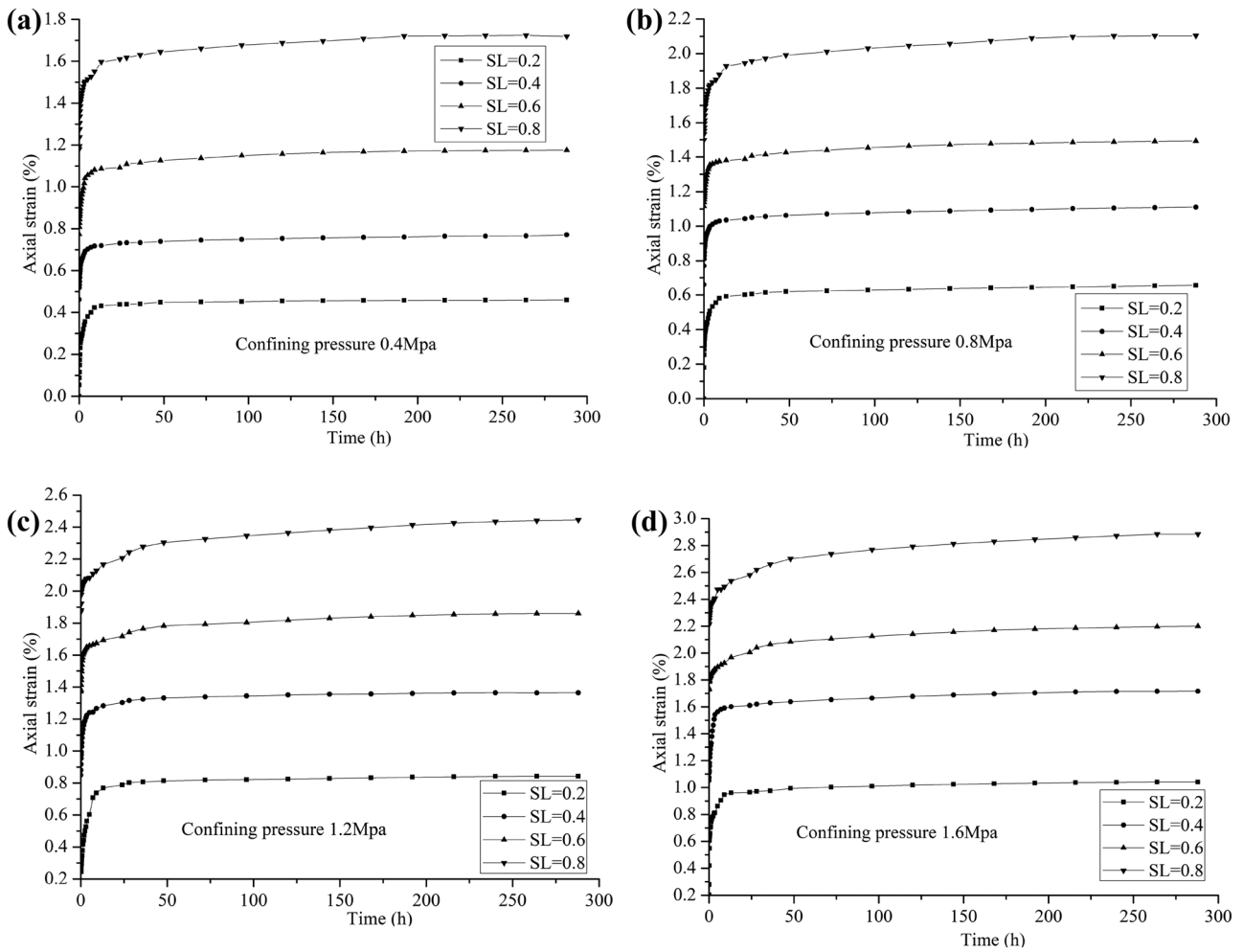
**Fig. 7** Strain–time relationship curves of triaxial creep tests (natural water content). **a** Confining pressure 0.4 MPa, sample N1; **b** confining pressure 0.8 MPa, sample N2; **c** confining pressure 1.2 MPa, sample N3; and **d** confining pressure 1.6 MPa, sample N4
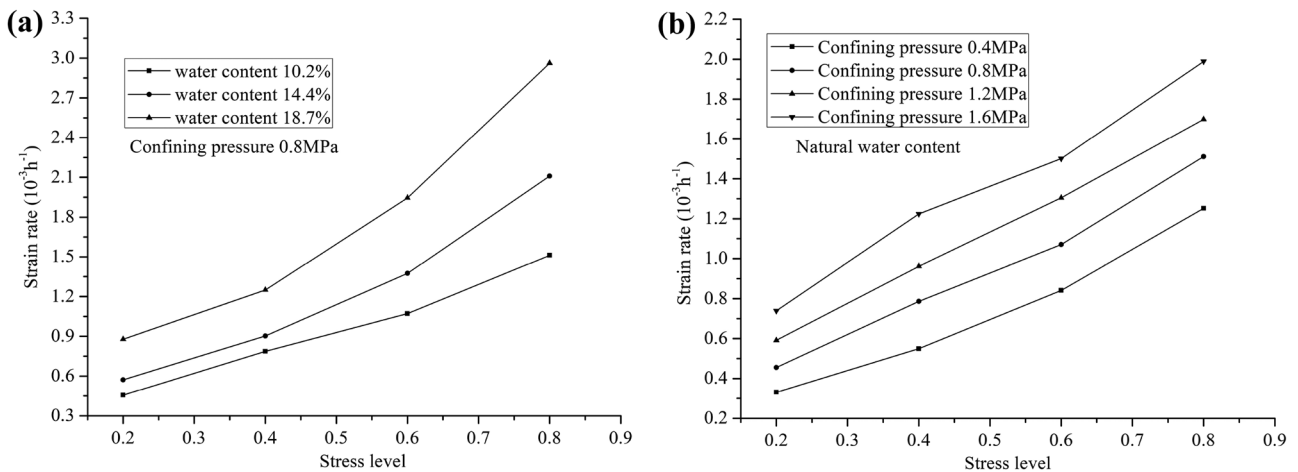


**Fig. 8** Strain rate–stress level relationship curves of triaxial creep tests. **a** Confining pressure 0.8 MPa, sample N2, N5, and N6; and **b** natural water content, sample N1, N2, N3, and N4
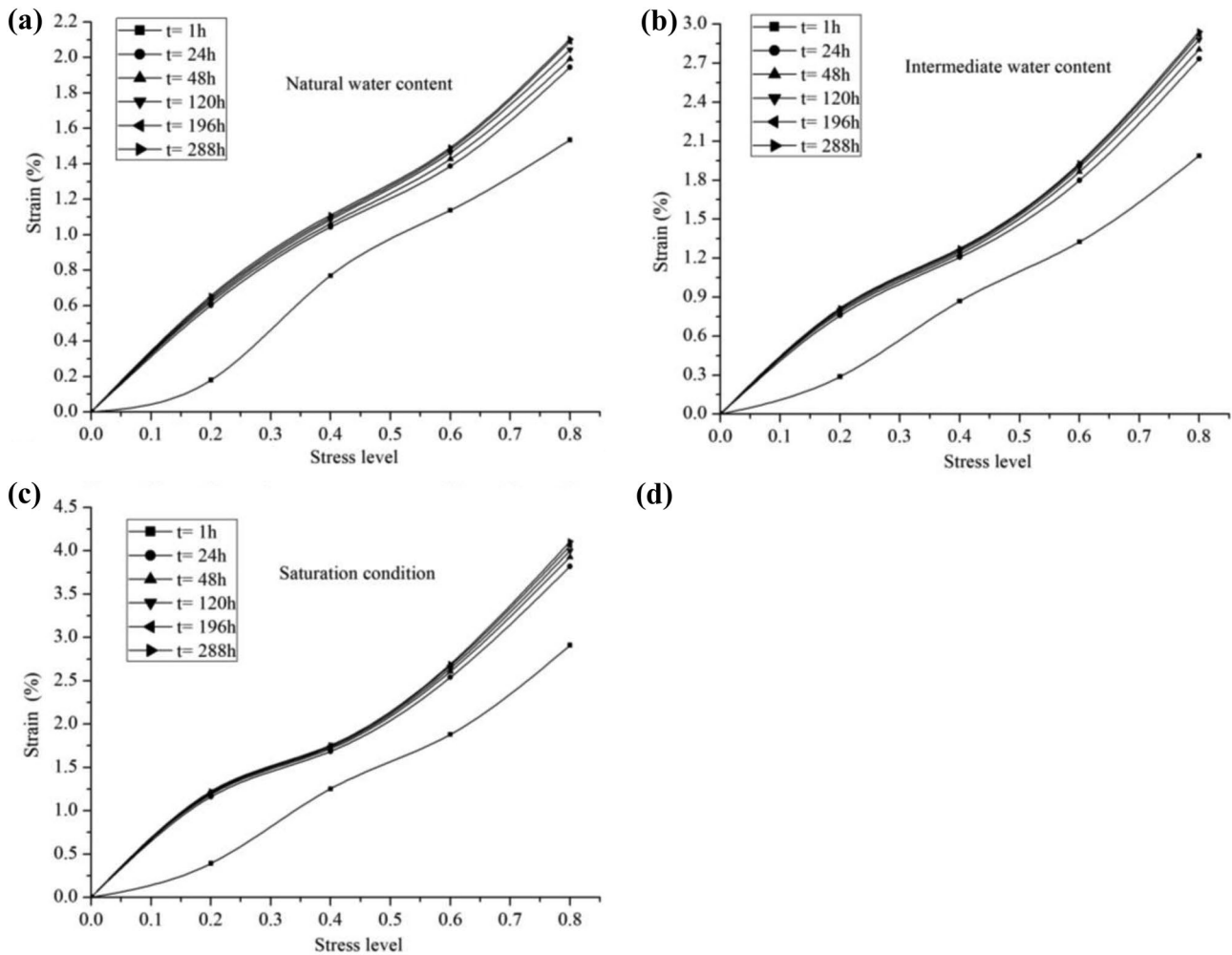
**Fig. 9** Stress level–strain curves under different water content, confining pressure 0.8 MPa. **a** Water content 11.0%, sample N2; **b** water content 18.0%, sample N5; and **c** water content 25.2%, sample N16

in this study. From the SEM observations (Fig. 11), it can be seen that the microscopic failure patterns are slightly different under before and after the creep test. There are more growing cracks, and the fracture surface is coarse with less micro grains before test. After the creep test, the porosity decreases with more micro grains on the fracture surface. During the testing process, microfissure damage inside the rock sample continuously accumulates, and then, the cracks, originating from the defects of initial internal voids, extend and interpenetrate, and eventually lead to the failure.

The particle and crack analysis system was introduced by Liu et al. (2011) to quantify and characterize micropore systems and is based on image processing. The non-destructive approach, which involves imaging, geometric and statistical measurement methods, was applied here to the SEM images of the red clay microstructures affected by testing.

Processing of the SEM images was implemented to quantify the features of the pore structures in the clay samples.

Binarization of the images was achieved by adaptive threshold segmentation, from which the void ratio and pore structure parameters were calculated. The image segmentation threshold was designated by a human operator, followed by automatic analysis, which has proven to be suitable and is convenient (Liu et al. 2011; Cui and Jia 2013). A minimum pore area of $S0 = 50$ (equivalent to 0.27 $\mu m^2$) was selected, resulting in pores < 50 pixels being either neglected or integrated into nearby large pores. The division radius ($r$) between the pores was 2.0 pixels.

Grayscale 500 × SEM images of the red clay are shown in Fig. 18. The porosity values before and after shearing are mostly within the range 50–120. The 500 × image magnification allows full identification of the soil microstructure and quantification of the porosity in the red clay before and after shearing. Taking Fig. 18a as an example, the selected porosity Tn is in the 0.34–0.36 range, which corresponds to a real grayscale range of 100–120.
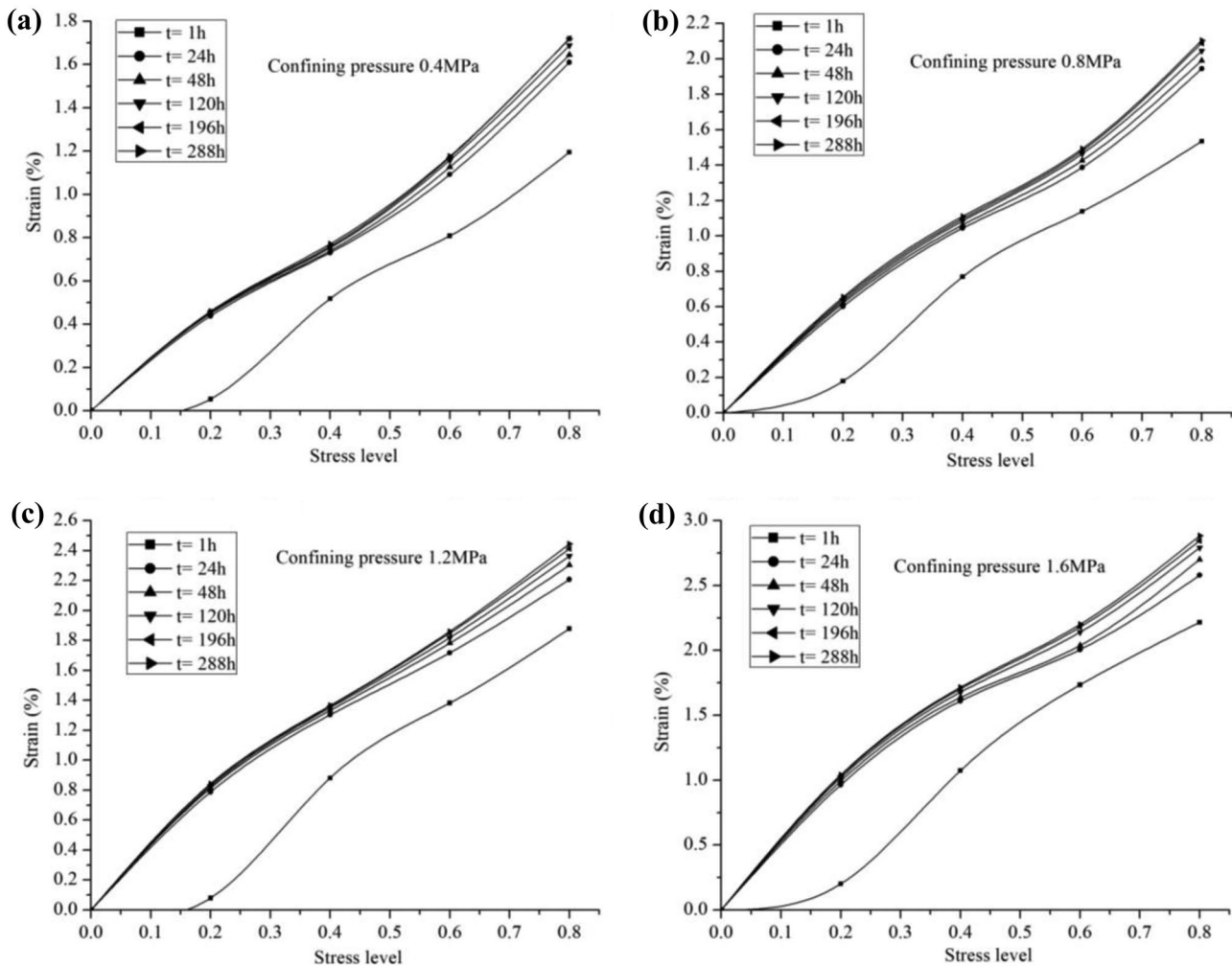
**Fig. 10** Stress level–strain curves under different confining pressure, natural water content. **a** Confining pressure 0.4 MPa, sample N1; **b** confining pressure 0.8 MPa, sample N2; **c** confining pressure 1.2 MPa, sample N3; and **d** confining pressure 1.6 MPa, Sample N4

A number of statistical parameters, such as pore area, average form factor, and fractal dimension, should be adopted to represent micropore features because the pore area changes across a wide range (Fig. 12). The statistical parameters of the SEM images at threshold values in the 100–120 Gy level range are provided in Table 3. The pore porosity probability distribution index can be applied to elucidate the pore area distribution characteristics, and the values of the five probability distribution indices are listed in Table 3.

## Creep model analysis

### The composite creep model

When any level of axial stress is applied (Fig. 5), the mudstone develops instantaneous elastic strain, indicating that the rheological model should contain elastic elements. Under a certain axial stress, the strain of the mudstone increases with time, indicating that the rheological model should incorporate viscous elements. In addition, viscoplastic elements should be included. Thus, the creep characteristics of the mudstone can be described reasonably and comprehensively by using the combined creep model (Yang and Cheng 2011; Yang et al. 2014; Liu and Zhang 2019). The combined creep model (Fig. 13) is composed of a Hooke body, a Kelvin body, and a viscoplastic body arranged in series. The mechanical model and the schedule of each creep phase are illustrated in Fig. 13. The creep strain curve is divided into four stages ($\varepsilon_1$, $\varepsilon_2$, $\varepsilon_3$, and $\varepsilon_4$), defined by points A–D (Fig. 13); the total strain is the sum of the stages.

The four creep strains and the total strain can be described by the following equations.
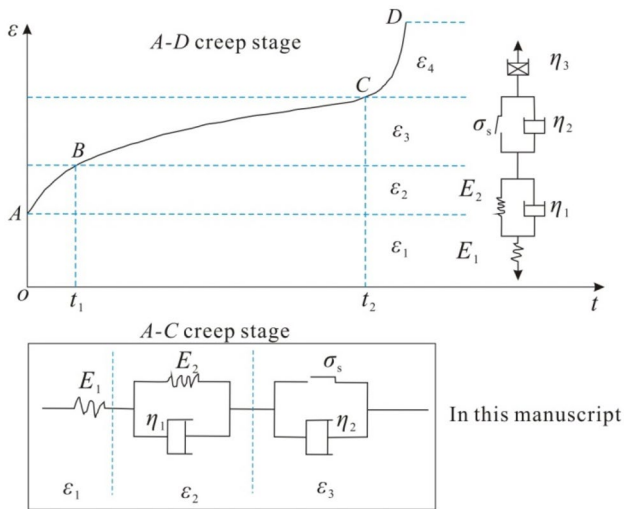
$$\varepsilon_1 = \frac{\sigma}{E_1} \tag{1}$$

$$\varepsilon_2 = \frac{\sigma}{E_2}\left(1 - exp\left(-\frac{E_2}{\eta_1}t\right)\right) \tag{2}$$

$$\varepsilon_3 = 0, \sigma < \sigma_s; \qquad \varepsilon_3 = \frac{\sigma - \sigma_s}{\eta_2}t, \ \sigma \geq \sigma_s \tag{3}$$

$$\varepsilon_4 = \frac{\sigma}{2\eta_3}\left(t - t_2\right)^2 \tag{4}$$

$$\varepsilon = \varepsilon_1 + \varepsilon_2 + \varepsilon_3 + \varepsilon_4 \tag{5}$$

where $\varepsilon_1$, $\varepsilon_2$, $\varepsilon_3$, and $\varepsilon_4$ are elastic strain, viscoplastic strain, Kelvin strain and nonlinear dashpot strain (damage strain), respectively; $\sigma_s$ is the Yield stress of the mudstone; $\sigma$ is the total stress; $\varepsilon$ is the total strain. $t$ is the creep time, $E_1$ is

**Fig. 11** Clay microstructure before and after the monotonic shear test. **a** Original state before creep test (50 μm). **b** Original state before creep test (10 μm). (c) After creep test (50 μm). **d** After creep test (10 μm)
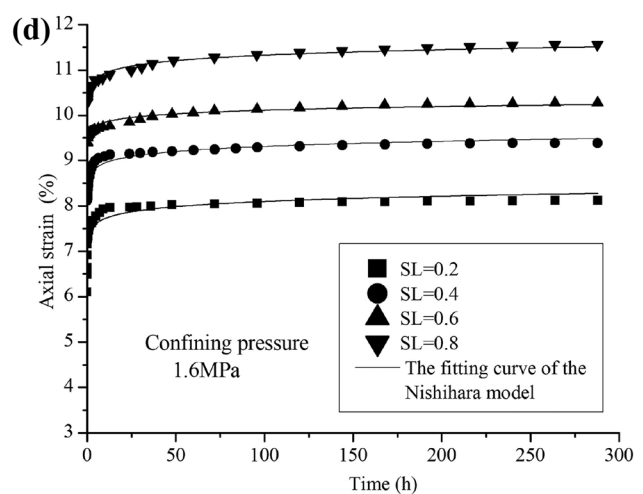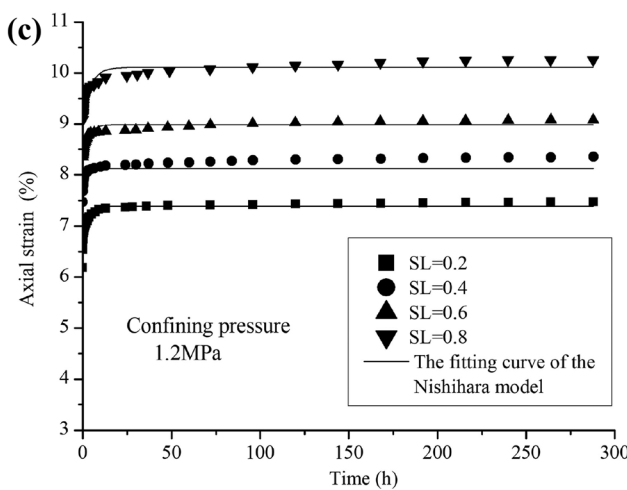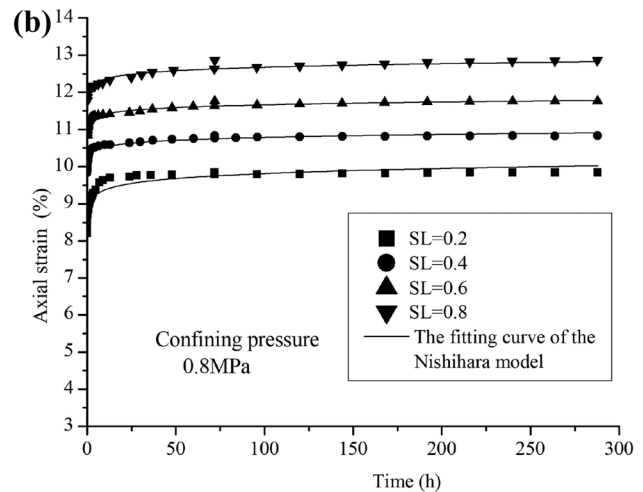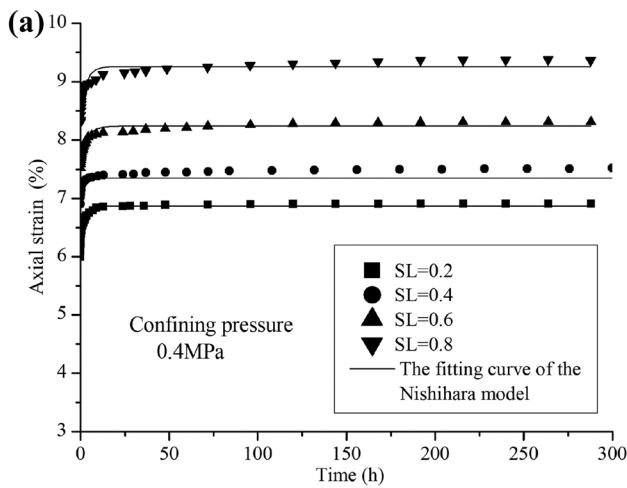


**Fig. 12** Pore structure processing of original clay and clay after creep test (the pore is white or other colors and soil particle is black). **a** Original clay SEM image (50 μm). **b** Original clay binary image with ample dots. **c** Original clay vectorization result. **d** SEM image (50 μm) after creep test. **e** Binary image after creep test. **f** Vectorization result after creep test

**Table 3** Some statistical parameters using the PCAS method

| Pore parameter | Original clay | Creep shear test |
|---|---|---|
| Image area/pixel | 1,228,800 | 1,228,800 |
| Total pore region area/pixel | 362,060 | 203,711 |
| Pore region number | 914 | 1034 |
| Pore region percentage (Porosity) | 29.46% | 16.58% |
| Pore maximum region area/pixel | 12,417 | 9255 |
| Pore average region area/pixel | 396.13 | 197.01 |
| Pore average perimeter/pixel | 114.23 | 81 |
| Pore average form factor | 0.3875 | 0.3633 |
| Pore maximum length/pixel | 280.02 | 417.48 |
| Pore average length/pixel | 30.82 | 23.54 |
| Pore maximum width/pixel | 152.28 | 101.54 |
| Pore average width/pixel | 17.01 | 12.67 |
| Pore probability entropy | 0.9873 | 0.9127 |
| Pore fractal dimension | 1.3117 | 1.269 |
| Pore area probability distribution index | 1.7622 | 2.2621 |
| Pore porosity distribution fractal dimension | 1.6797 | 2.5169 |
| Sorting coefficient | 1.324089 | 1.347234 |
| Uniformity coefficient | 1.552938 | 2.006943 |
| Curvature coefficient | 1.105730 | 1.409321 |
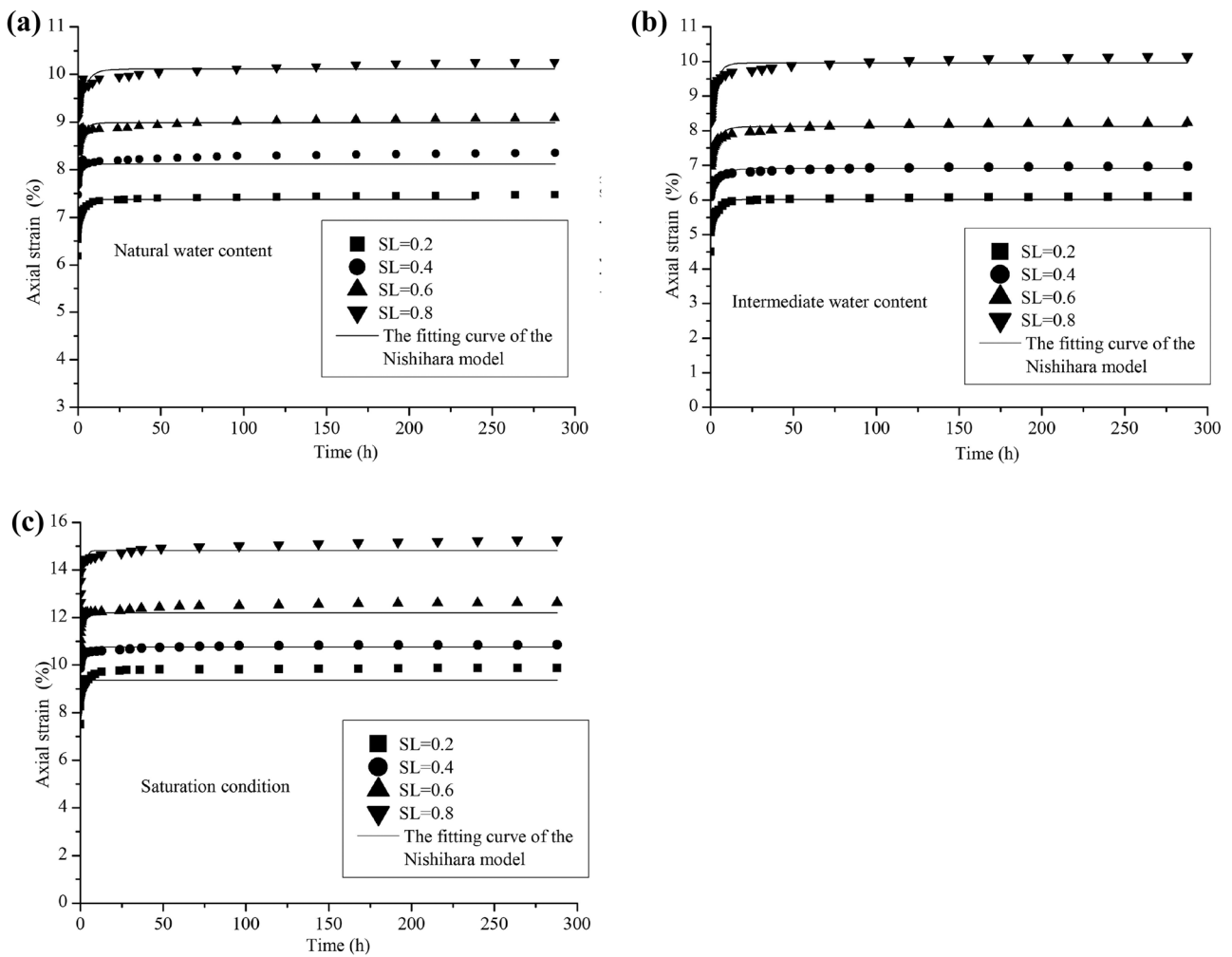


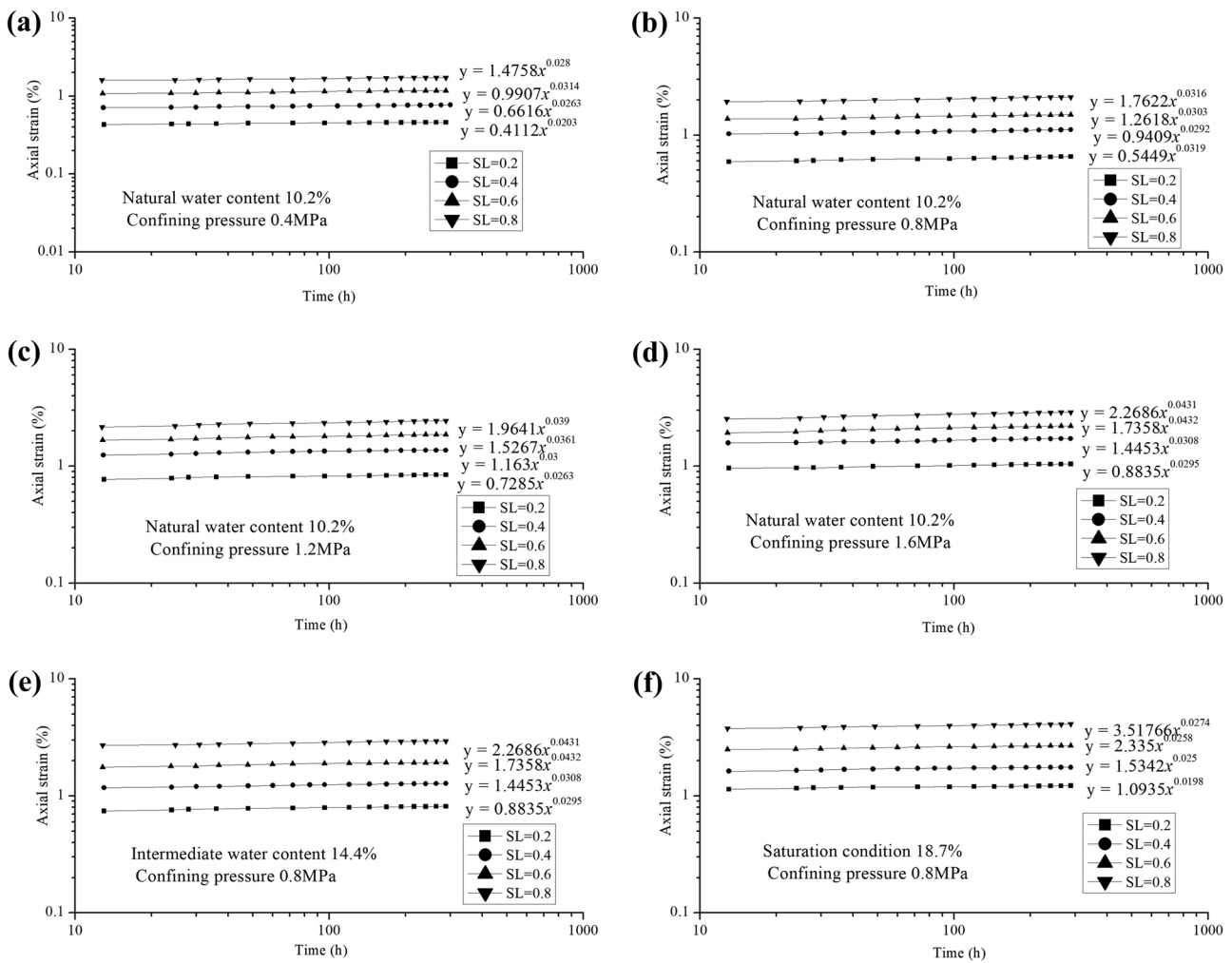**Fig. 13** The composite creep model

**Fig. 14** Creep curves and composite model fitting results of mudstone under different confining pressures. **a** Confining pressure 0.4 MPa, sample N1; **b** confining pressure 0.8 MPa, sample N2; **c** confining pressure 1.2 MPa, sample N3; and **d** confining pressure 1.6 MPa, sample N4

the instantaneous elasticity modulus, $E_2$ is the viscoelastic modulus; and $\eta_1$ and $\eta_2$ are viscoelastic coefficients.

Formula (6) can be obtained from Eqs. (1)–(5): when $\sigma < \sigma_s$,

$$\varepsilon = \frac{\sigma}{E_1} + \frac{\sigma}{E_2}\left(1 - exp\left(-\frac{E_2}{\eta_1}t\right)\right)$$

when $\sigma \geq \sigma_s$, $t < t_2$

$$\varepsilon = \frac{\sigma}{E_1} + \frac{\sigma}{E_2}\left(1 - exp\left(-\frac{E_2}{\eta_1}t\right)\right) + \frac{\sigma - \sigma_s}{\eta_2}t$$

when $\sigma \geq \sigma_s$, $t \geq t_2$

$$\varepsilon = \frac{\sigma}{E_1} + \frac{\sigma}{E_2}\left(1 - exp\left(-\frac{E_2}{\eta_1}t\right)\right) + \frac{\sigma - \sigma_s}{\eta_2}t + \frac{\sigma}{2\eta_3}\left(t - t_2\right)^2$$

(6)

In this study, the mudstone creep behavior in the tests was applied to the curve between points A and C of Fig. 13. The following creep model can be used:

$$\varepsilon = \frac{\sigma}{E_1} + \frac{\sigma}{E_2}\left(1 - exp\left(-\frac{E_2}{\eta_1}t\right)\right) + \frac{\sigma - \sigma_s}{\eta_2}t, \ \sigma \geq \sigma_s, \ t < t_2$$

The parameters of the creep model can be fitted by the time period of the creep stage using the graphing software Origin to fit the test results according to the composite model. The fitting curves (Figs. 14 and 15) and the associated parameters were determined for the composite model (Table 4). By comparing the creep curves we found that the strain–time relationship obtained by the composite model is consistent with the test results. Thus, the composite model can express well the time-dependent behavior of the mudstone as well as the transient and steady creep.
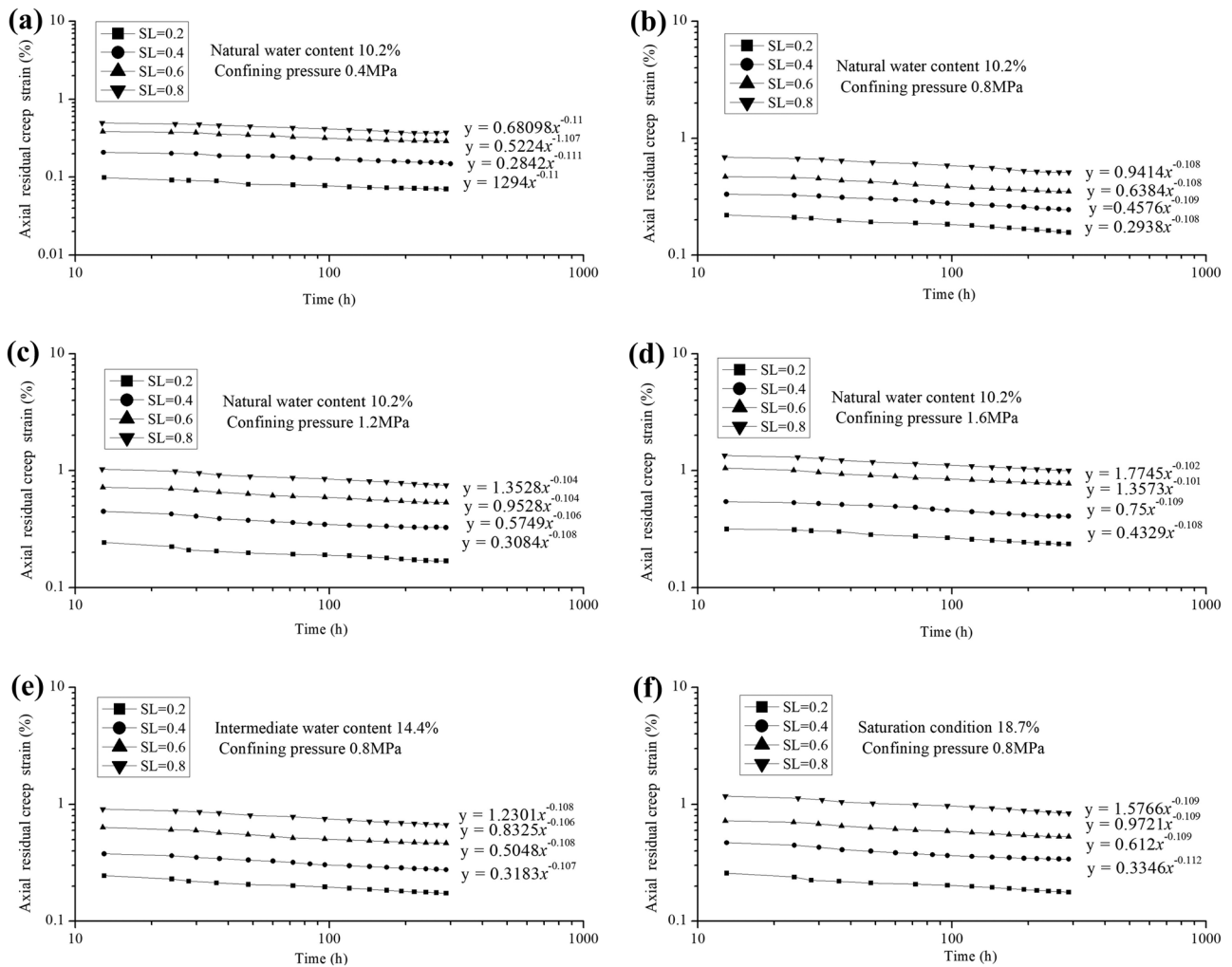
**Fig. 15** Creep curve and composite model fitting results of mudstone under different moisture content. **a** Water content 11.0%, sample N2; **b** water content 18.0%, sample N5; and **c** water content 25.2%, sample N16

## A new creep model

According to the theory of hysteresis deformation, the total strain $\varepsilon$ in the creep process can be divided into the instantaneous elastic–plastic strain $\varepsilon_{ep}$ and the hysteresis viscous strain $\varepsilon_L(t)$ (Singh and Mitchell 1968; Mesri et al. 1981).

$$\varepsilon = \varepsilon_{ep} + \varepsilon_L(t) \tag{7}$$

where $\varepsilon_{ep}$ can be calculated by any existing elastoplastic model.

The relationship between creep strain and time is linear in a log–log coordinate system. The "residual creep strain" $\varepsilon_f - \varepsilon_L$ also has a linear relationship with time in a log–log coordinate system. A power function can be used to express the creep strain–time curve:

$$\varepsilon_L = \varepsilon_f(1 - t^{-\lambda}) \tag{8}$$

The temporal axial strain curves of mudstone under different stress states are plotted in Fig. 16. All the curves show a linear relationship on the log–log graph. This result is in agreement with the assumption about the axial strain–time relation of soils in the Mesri creep model (Mesri et al. 1981; Mesri and Choi 1984; Jiang et al. 2014). In logarithmic coordinates, the strain increases slowly with time and gradually becomes stable.

The strain at $t = 12$ (h) is obtained as the initial elastic–plastic strain $\varepsilon_{ep}$, which can be obtained by combining the transformation of Eqs. (7) and (8):

$$(\varepsilon_f + \varepsilon_{ep}) - \varepsilon = \varepsilon_f \cdot t^{-\lambda} \tag{9}$$

**Table 4** Parameters derived from composite model

| Experimental conditions | Stress level | Axial strain (MPa) | $E_1$(MPa) | $E_2$(MPa) | $\eta_1$(MPah) | $\eta_2$(MPah) | $R^2$ (fitting curve correlation coefficient) |
|---|---|---|---|---|---|---|---|
| Confining pressure 0.4 MPa | 0.2 | 0.08 | 0.011577 | 0.181768 | 0.355281 | 1.24358 | 0.95951 |
| | 0.4 | 0.16 | 0.02099 | 0.259243 | 0.952784 | | 0.92772 |
| | 0.6 | 0.24 | 0.039157 | 0.324107 | 0.571868 | | 0.94906 |
| | 0.8 | 0.32 | 0.037776 | 0.406441 | 1.308825 | | 0.90332 |
| Confining pressure 0.8 MPa | 0.2 | 0.16 | 0.024409 | 0.192352 | 0.373006 | 3.42369 | 0.90452 |
| | 0.4 | 0.32 | 0.042941 | 0.488824 | 1.263529 | | 0.91086 |
| | 0.6 | 0.48 | 0.056996 | 0.848347 | 2.754311 | | 0.91843 |
| | 0.8 | 0.64 | 0.069254 | 0.734671 | 3.50283 | | 0.9182 |
| Confining pressure 1.2 MPa | 0.2 | 0.24 | 0.03344 | 0.371601 | 0.82436 | 4.02358 | 0.91254 |
| | 0.4 | 0.48 | 0.057535 | 0.154755 | 2.139036 | | 0.94356 |
| | 0.6 | 0.72 | 0.227914 | 1.039803 | 1.661616 | | 0.95036 |
| | 0.8 | 0.96 | 0.124644 | 1.195189 | 4.208034 | | 0.90536 |
| Confining pressure 1.6 MPa | 0.2 | 0.16 | 0.024434 | 0.193474 | 0.35736 | 5.42365 | 0.9023 |
| | 0.4 | 0.32 | 0.042835 | 0.488655 | 0.000125 | | 0.91365 |
| | 0.6 | 0.48 | 0.056985 | 0.848455 | 2.754906 | | 0.93025 |
| | 0.8 | 0.64 | 0.069249 | 0.73467 | 3.502854 | | 0.95357 |
| Natural water content | 0.2 | 0.16 | 0.032201 | 0.153439 | 0.413456 | 4.1568 | 0.91086 |
| | 0.4 | 0.32 | 0.05156 | 0.458615 | 2.359784 | | 0.91843 |
| | 0.6 | 0.48 | 0.067595 | 0.472209 | 1.942835 | | 0.9182 |
| | 0.8 | 0.64 | 0.076066 | 0.415422 | 1.401547 | | 0.90124 |
| Intermediate water content | 0.2 | 0.16 | 0.021338 | 0.085914 | $3.05E-06$ | 1.70236 | 0.92374 |
| | 0.4 | 0.32 | 0.032137 | 0.39559 | 0.895014 | | 0.97121 |
| | 0.6 | 0.48 | 0.044195 | 0.355959 | 0.000107 | | 0.95367 |
| | 0.8 | 0.64 | 0.049693 | 0.331373 | 0.04393 | | 0.9505 |
| Saturated condition | 0.2 | 0.16 | 0.024434 | 0.193474 | 0.35736 | 0.05126 | 0.8356 |
| | 0.4 | 0.32 | 0.042835 | 0.488655 | 0.000125 | | 0.9306 |
| | 0.6 | 0.48 | 0.056985 | 0.848455 | 2.754906 | | 0.8321 |
| | 0.8 | 0.64 | 0.069249 | 0.73467 | 3.502854 | | 0.8717 |

From the measurements of creep strain $\varepsilon_{ep}$, $\varepsilon$ and time $t$ obtained in the creep tests, $\varepsilon_f$ and $\lambda$ are obtained by fitting the test data (Fig. 17). The following formula can be obtained.

$$(\varepsilon_f + \varepsilon_{ep}) - \varepsilon = \varepsilon_f - \varepsilon_L$$

where $\varepsilon_f - \varepsilon_L$ is the residual creep. The curve of $\varepsilon_f - \varepsilon_L$ vs. $t$ is linear in a log-log coordinate system. $\varepsilon_f$ and $\lambda$ are a function of the stress state.

(1) Relationship between $\varepsilon_f$ and the stress state

The relationship between εf and σ3 of mudstone at different stress levels (Fig. 18a) is linear and can be expressed as:

$$\varepsilon_f = \alpha + \beta \cdot \sigma_3 \tag{10}$$

The relationship between the soil coefficients $\alpha$ and $\beta$ and the stress level $S_L$ are illustrated in Fig. 18b. The relationship between $\alpha$ and $S_L$ can be expressed as a power function, and that between $\beta$ and $S_L$ can be expressed by a hyperbolic function. The derived fitting curve is consistent with the experimental results.

$$\alpha = a \cdot s_L^{\ b}$$
$$\beta = \frac{c \cdot s_L}{1 - d \cdot s_L} \tag{11}$$

The relationship between $\varepsilon_f$ and the stress state can be obtained by substituting Eq. (8) into Eq. (10).

$$\varepsilon_f = a \cdot s_L^{\ b} + \frac{c \cdot s_L}{1 - d \cdot s_L} \sigma_3 \tag{12}$$

where a, b, c, and d are dimensionless parameters.

(2) Relationship between $\lambda$ and the stress state

The fitting curve of $\lambda$ and $\sigma_3$, which can be expressed as a power function relation, is plotted in Fig. 18c.

**(a)**



**(b)**

$\beta = 1.1671 S_L / (1 - 0.145 S_L)$

$\alpha = 0.3137 S_L^{1.0132}$

**(c)**

$\lambda = 0.10854 \sigma_3^{-0.02134}$

$\lambda = 0.10819 \sigma_3^{-0.01903}$

$\lambda = 0.10603 \sigma_3^{-0.03288}$
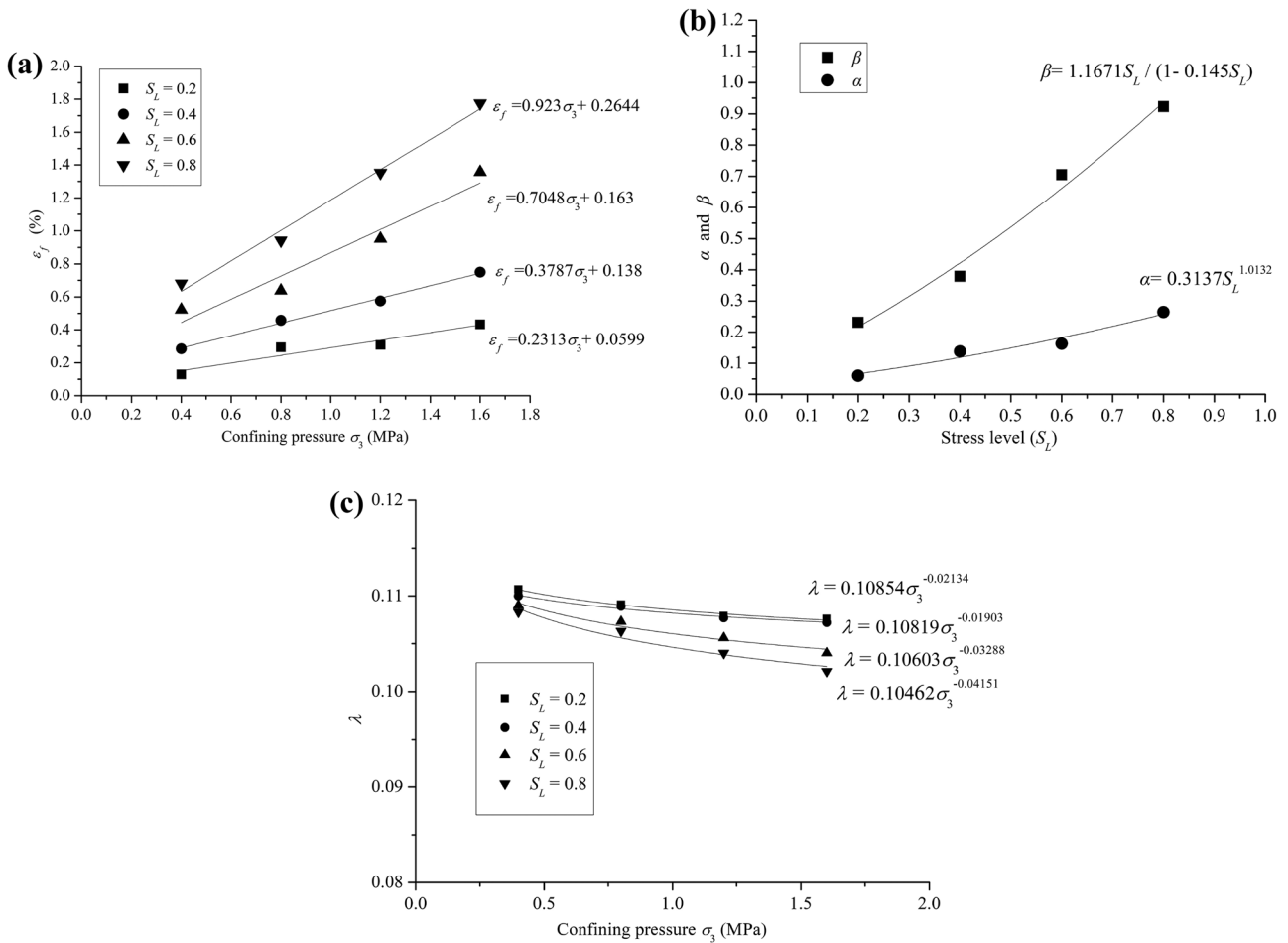
$\lambda = 0.10462 \sigma_3^{-0.04151}$

**Fig.16** Mudstone creep $\varepsilon \sim t$ curve (exponential fitting)

$$\lambda = \eta \cdot \sigma_3^{-m} \tag{13}$$

Therefore, Eqs. (9), (11), and (13) and parameters *a*, *b*, *c*, *d*, *m* and *η*, provide a complete description of the characteristics of the axial strain creep of mudstone.

In conclusion, by analyzing the functional relationship between strain and time in mudstone creep behavior, we established a creep model for mudstone in Tianshui, Gansu Province. Analysis of the creep curves and model parameters showed that both the composite model and the new creep model reflect the creep characteristics of this mudstone.

From the experimental results, the composite creep model has the following characteristics. When the shear stress is less than the long-term strength, the strain rate gradually decreases through time and approaches an asymptote, which can be simulated by the Kelvin model. However, the rheological curve described by a single Kelvin model is relatively gentle at the beginning. Addition of more Kelvin models in series causes the rheological curve to rise faster, consistent

with the initial rheological deformation of clay rock. However, too many models result in a larger number of undetermined coefficients, making the model difficult to apply to engineering practice. Therefore, the model proposed in this paper describes the rheological deformation characteristics of clay-rich rock in the viscoelastic stage. When the shear stress is greater than the long-term strength, the rheology of the clay rock will appear constant. The proposed model also performs well in describing the rock's linear viscoplastic properties. Moreover, the proposed model reflects the residual creep characteristics of the mudstone in the study area. The new model can reflect both axial and volumetric creep.

Other studies have considered damage mechanisms under osmotic and high confining pressures. The experiment conducted in this paper differs from those of previous studies in that the steady creep of mudstone under low confining pressure but with different water contents is considered, as a way of modeling the actual engineering situation. The results are applied to establish a stable creep model that characterizes the mudstone under low confining
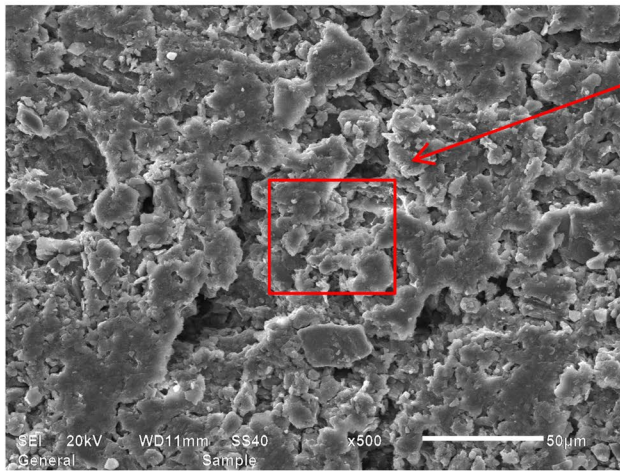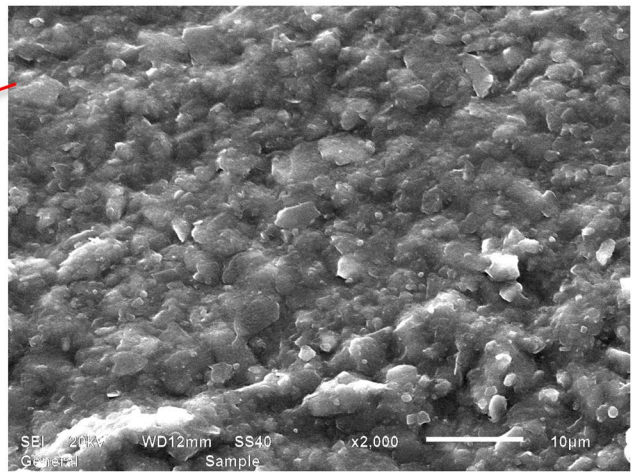
**(a)** original state before creep test (50 $\mu$m)
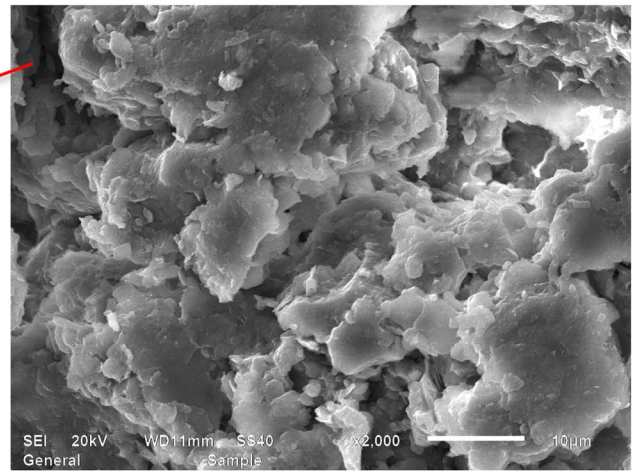


**(b)** original state before creep test (10 $\mu$m)
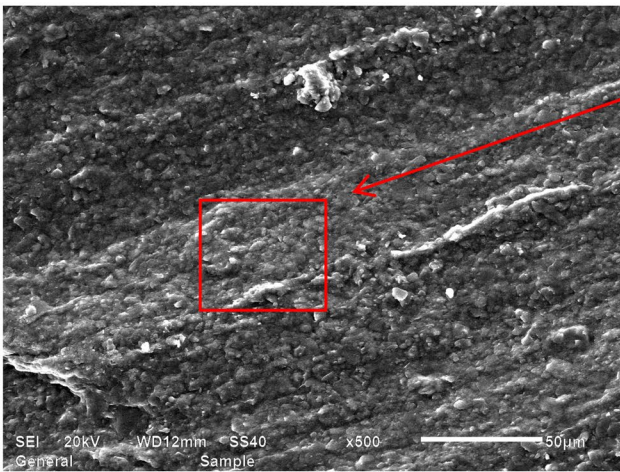


**(c)** After creep test (50 $\mu$m)



**(d)** After creep test (10 $\mu$m)

**Fig. 17** Mudstone creep $(\varepsilon_f - \varepsilon_L) \sim t$ curve (exponential fitting)

pressure. That the model is only useful for low confining pressure is a limitation of this study. Shear creep is one of the main factors in landslide occurrence, and the shear creep mechanical model of mudstone can explain the phenomenon of mudstone landslides. The stress–strain–time model of creep deformation of mudstone established in this paper has few parameters and a simple derivation process, thus providing a new means of evaluating slope long-term stability. The model could also be applied to predict impending landslides.

In this study, the creep tests of slope mudstone were designed considering the engineering geological conditions. The exponential empirical model is expressed by using the relationship between residual creep and time. The data points of the creep constitutive model are basically consistent with the measured values, and the accuracy is better than the previous model (Figs. 14, 15, 16, and 17). The constitutive model proposed in this paper performs well in describing the creep deformation of mudstone in the Tianshui area.

## Discussions

From the perspective of microscopic analysis, there are two reasons for soil creep (Lade and Liu 1998; Augustesen et al. 2004; Liingaard et al. 2004; Karimpour and Lade 2010, 2013; Gao et al. 2012). One reason is that under increasing load, soil mineral particles or mineral clusters continuously slide and rotate with time, and their spatial positions are
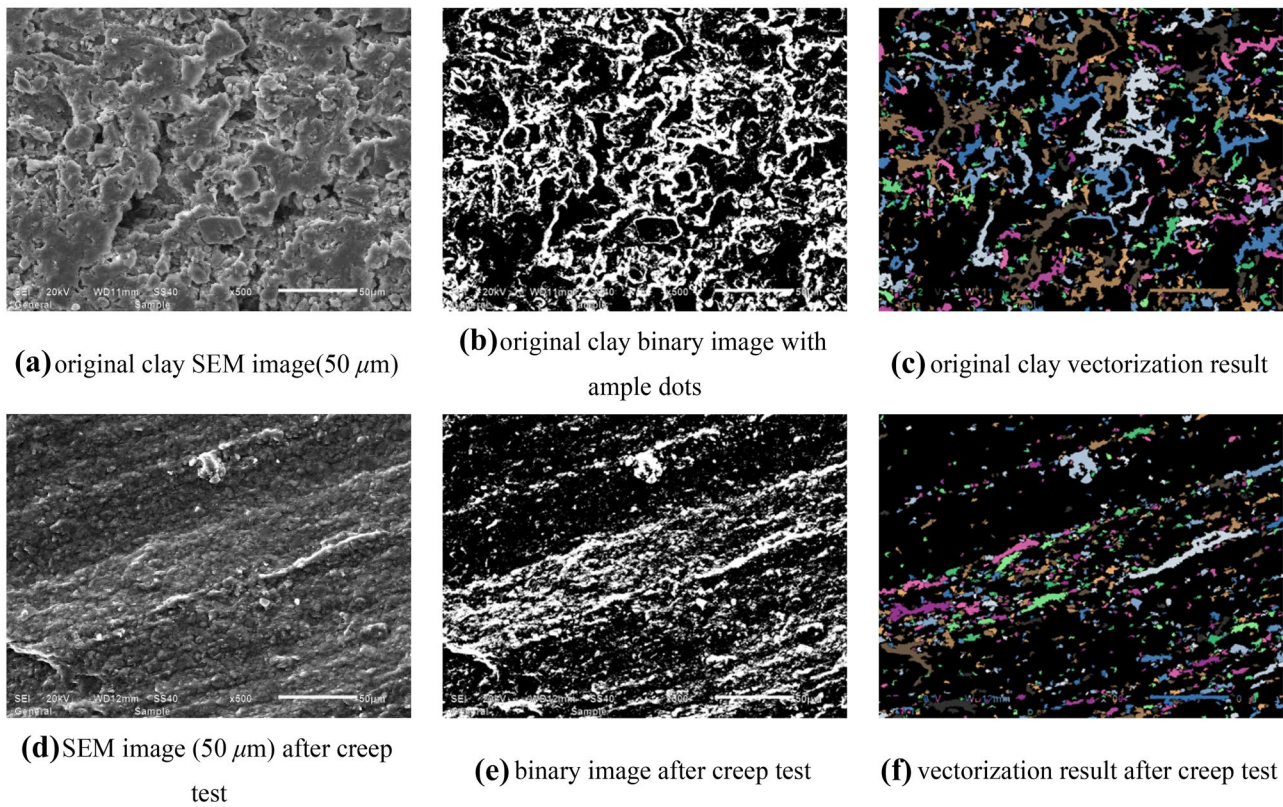
**(a)** original clay SEM image(50 $\mu$m)

**(b)** original clay binary image with ample dots

**(c)** original clay vectorization result

**(d)** SEM image (50 $\mu$m) after creep test

**(e)** binary image after creep test

**(f)** vectorization result after creep test

**Fig. 18** Creep index for the model. **a** Creep index $\varepsilon_f \sim \sigma_3$ curves of creep tests under natural water content; **b** creep index $\alpha$ and $\beta \sim S_L$ curves of creep tests under natural water content, confining pressure 0.8 MPa; and **c** creep index $\lambda \sim \sigma3$ curves of creep tests under natural water content

constantly adjusted. The other reason is that failure of mineral particles or clusters occurs at the corner point of the stress concentration under a constant load. The highest shear stress used in our test was 0.96 MPa, a value much smaller (by an order of magnitude) than that required to cause failure of the mineral particles in the soil. Therefore, the creep mechanism in the mudstone samples is mainly related to the relative movement and rotation of the microscopic particles.

At the initial stage of sample loading, the load increases continuously in a short period of time, and the spatial position of the mineral particles and mineral clusters is constantly changing. As uneven stress fills the soil pores, the porosity of the soil continues to decrease, and macroscopically, the creep rate increases. The contact coordination number of the mineral particles continues to increase and the relative rotation and mutual slip of the particles decreases. Macroscopically, the creep rate of the soil mass decreases constantly. When the coordination number of the particles reaches a certain value, a stable stress chain is formed between the particles, and the position of the mineral particles is only slightly adjusted, so that the rate of the macroscopic deformation of the soil becomes stable.

Thus, the rate and magnitude of the creep are closely related to the adjustment range of the position of the fine particles, and the adjustment range of the particles is related to the shear stress value. Therefore, the absolute creep value, creep rate and creep stage of the soil are all related to the shear stress value or shear stress level.

## Conclusions

In this study, creep tests were carried out to investigate the shear and creep behavior of mudstone at different confining pressures, stress level, and water content. Particular attention was paid to creep failure time and strain rate in creep tests. The following conclusions can be drawn:

(1)  The mudstone creep increases slowly through time and with rising stress level, but eventually achieves a stable value. The creep increases with increasing stress difference, confining pressure, and water content. The microscopic features show Carnisaw soil structure evolution with a flocculated structure controlled by edge-to-face particle associations. SEM images of clay obtained

from specimens subjected to shear tests indicate that the bonding of the red soil was weakened by shearing, and the microstructure changed markedly.

(2) A new creep model was established to elucidate the creep deformation mechanism of the Tianshui mudstone landslides. The new model, which is based on a power function formula, reflects the creep characteristics of the mudstone samples better than previous models. The axial strain of the mudstone samples has a linear relationship with time on a log–log graph under different stress states. The strain increases slowly with time and gradually stabilizes. The proposed model reflects the residual creep characteristics of the mudstone. Moreover, the mode can reflect both axial and volumetric creep.

## Declarations

**Conflict of interest** We declare that we have no financial and personal relationships with other people or organizations that can inappropriately influence our work. There is no professional or other personal interest of any nature or kind in any product, service, and/or company that could be construed as influencing the position presented in, or the review of, the manuscript entitled.

## References

Adaehi T, Oka F, Koike M (2005) An elasto-viscoplastic constitutive model withstrain-softening for soft sedimentary rocks. Soils Found 45(2):125–133

Al-Rawas AA, McGown A (1999) Structure of Omani expansive soils. Can Geotech J 36:272–290

Augustesen A, Liingaard M, Lade PV (2004) Evaluation of time-dependent behavior of soils. Int J Geomech 4(3):137–156

Bozzano F, Martino S, Montagna A (2012) A back analysis of a rock landslide to infer rheological parameters. Eng Geol 131–132:45–56

Bizjak KF, Zupančič A (2009) Site and laboratory investigation of the Slano blato landslide. Eng Geol 105:171–185

Bonini M, Debernardi D, Barla M, Barla G (2009) The mechanical behaviour of clay shales and implications on the design of tunnels. Rock Mech Rock Eng 42:361–388

Coll C, Collin F, Radu JP, Illing P, Schroeder Ch, Charlier R (2006) The report of long term behavior of Boom clay-influence of clay viscosity on the far field pore pressure distribution. EURIDICE 154.

Cui YJ, Le TT, Tang AM, Delage P, Li XL (2009) Investigating the time-dependent behavior of Boom clay under thermo-mechanical loading. Géotechnique 4:319–348

Cui ZD, Jia YJ (2013) Analysis of electron microscope images of soil pore structure for the study of land subsidence in centrifuge model tests of high-rise building groups. Eng Geol 164(12):107–116

Enomoto T, Koseki J, Tatsuoka F (2015) Creep failure of sands exhibiting various viscosity types and its simulation. Soils Found 55(6):1346–1363

Gao HM, Chen YM, Liu HL, Liu JY, Chu J (2012) Creep behavior of EPS composite soil. SCIENCE CHINA Technol Sci 55(11):3070–3080

Giraud A, Rousset G (1996) Time-dependent behavior of deep clays. Eng Geol 41:181–195

Gasc-Barbier M, Chanchole S, Bérest P (2004) Creep behavior of Bure clayey rock. Appl Clay Sci 26:449–458

Guo Z, Wang Q, Yin S et al (2019) The creep compaction behavior of crushed mudstones under the step loading in underground mining. Int J Coal Sci Technol 6(3):408–418

Jiang MJ, Liu JD, Yin ZY (2014) Consolidation and creep behaviors of two typical marine clays in China. China Ocean Engineering 28(5):629–644

Karimpour H, Lade PV (2010) Time effects relate to crushing in sand. Journal of Geotechnical and Geoenvironmental Engineering 136(9):1209–1219

Karimpour H, Lade PV (2013) Creep behavior in Virginia beach sand. Can Geotech J 50(11):1159–1178

Li J, Yang Y (2018) Creep behavior of unsaturated reticulate red clay under matric suction. KSCE J Civ Eng 22(2):582–587

Lade PV, Liu C (1998) Experimental study of drained creep behavior of sand. J Eng Mech 124(8):912–920

Liingaard M, Augustesen A, Lade PV (2004) Characterization of models for time-dependent behavior of soils. Int J Geomech 4(3):157–177

Lin B, Cerato AB (2014) Applications of SEM and ESEM in microstructural investigation of shale-weathered expansive soils along swelling-shrinkage cycles. Eng Geol 177:66–74

Liu WB, Zhang SG (2019) Creep Parameter Determination and Model Establishment Considering Stress and Time Effects. Geotech Geol Eng. https://doi.org/10.1007/s10706-019-01106-6

Liu C, Shi B, Zhou J, Tang C (2011) Quantification and characterization of microporosity by image processing, geometric measurement and statistical methods: application on SEM images of clay materials. Appl Clay Sci 54(1):97–106

Mesri G, Rebres-Cordero E, Shields DR (1981) Shear stress-strain-time behavior of clays. Geotechnique 31(4):537–552

Mesri G, Choi YK (1984) Discussion of "Time effects on the stress-strain behaviours of natural soft clays." Géotechnique 34(3):439–442

Naumann M, Hunsche U, Schulze O (2007) Experimental investigations on an isotropy in dilatancy, failure and creep of Opalinus Clay. Phys Chem Earth 32:889–895

Pellet F, Hajdu A, Deleruyelle F, Besnus FA (2005) Visco-plastic model including anisotropic damage for the time dependent behaviour of rock. Int J Numer Anal Meth Geomech 29:941–970

Romero E, Simms PH (2008) Microstructural investigation in unsaturated soils: a review with special attention to contribution of mercury intrusion porosimetry and environmental scanning electron microscopy. Geotech Geol Eng 26:705–727

Rutter EH, Green S (2011) Quantifying creep behaviour of clay-bearing rocks below the critical stress state for rapid failure: Mam Tor landslide, Derbyshire, England. J Geol Soc Lond 168:359–372

Sergeyev YM, Grabowska-Olszewska B, Osipov VI, Sokolov VN, Kolomenski YN (1980) The classification of microstructures of clay soils. J Microsc 120:237–260

Singh A, Mitchell JK (1968) General stress-strain-time function for soils. Journal of Soil Mechanics and Found Engineering Division, ASCE 94(1):21–46

Sun M, Tang H, Wang M, Shan Z, Hu X (2016) Creep behavior of slip zone soil of the Majiagou landslide in the Three Gorges area. Environmental Earth Sciences 75(16):1199

Wen BP, Jiang XZ (2017) Effect of gravel content on creep behavior of clayey soil at residual state: implication for its role in slow-moving landslides. Landslides 14:559–576

Wen BP, Aydin A (2003) Microstructural study of a natural slip zone: quantification and deformation history. Eng Geol 68(3):289–317

Wang X, Hu B, Tang H, H, X., Wang, J., Huang, L., (2016) A constitutive model of granite shear creep under moisture. J Earth Sci 27:677–685

Wang X, Huang L, Yan C, Lian B (2018) HKCV rheological constitutive model of mudstone under dry and saturated conditions. Advances in Civil Engineering 6:1–10

Wang X, Huang L, Zhang J (2019) A rheological model of sandstones considering response to thermal treatment. Advances in Civil Engineering 3:1–9

Wang Z, Shi F, Zhang J (2020) Effects of Water on the Rheology of Dominant Minerals and Rocks in the Continental Lower Crust: A Review. J Earth Sci 31:1170–1182

Wang Y, Cong L, Yin X, Yang X, Xiong W (2021) Creep behaviour of saturated purple mudstone under triaxial compression. Eng Geol 288(3):106159

Wen BP, He L (2012) Influence of lixiviation by irrigation water on residual shear strength of weathered red mudstone in Northwest China: implication for its role in landslides' reactivation. Eng Geol 151:56–63

Yan S, Xiang W, Tang H, Man Z, Xu R (2008) Research on creep behavior of slip band soil of Dayantang landslide. Rock SoilMech 29(1):58–68

Yang SQ, Cheng L (2011) Non-stationary and nonlinear visco-elastic shear creep model for shale. Int J Rock Mech Min Sci 48(6):1011–1020

Yang W, Zhang Q, Li S, Wang S (2014) Time-dependent behavior of diabase and a nonlinear creep model. Rock Mech Rock Eng 47(4):1211–1224

Yu HD, Chen WZ, Gong Z, Tan XJ, Ma YS, Li XL, Sillen X (2015) Creep behavior of boom clay. Int J Rock Mech Min Sci 76:256–264

Zhang Y, Xu WY, Shao JF, Zhao HB, Wang W (2015) Experimental investigation of creep behavior of clastic rock in Xiangjiaba Hydropower Project. Water Science and Engineering 8(1):55–62

Zhang Z, Wang T, Wu S, Tang H, Xin P, Liang C (2017a) Dynamics stress–strain behavior of Tianshui soils. Landslides 14:323–335

Zhang Z, Wang T, Wu S, Tang H, Liang C (2017b) The role of seismic triggering in a deep-seated mudstone landslide, China: Historical reconstruction and mechanism analysis. Eng Geol 226:122–135

Zhang Z, Wang T, Wu S, Tang H, Liang C (2017c) Seismic performance of loess-mudstone slope in Tianshui – Centrifuge model tests and numerical analysis. Eng Geol 222:225–235